Title

Mechanoadaptive strain and functional osseointegration of dental implants in rats

Authors

Wang, B

Kim, K

Srirangapatanam, S

et al.

Publication Date

2020-08-01

DOI

10.1016/j.bone.2020.115375

Peer reviewed

Mechanoadaptive Strain and Functional Osseointegration of Dental Implants in Rats

B. Wang[1*], K. Kim[1*], S. Srirangapatanam[2], P. Ustriyana[1], S. E. Wheelis[3], S. Fakra[4], M. Kang[1], D. C. Rodrigues[3], S. P. Ho[1, 2, #]

[1]Department of Preventive and Restorative Dental Sciences, School of Dentistry, UCSF, San Francisco, CA 94143

[2]Department of Urology, School of Medicine, UCSF, San Francisco, CA 94143

[3]Department of Bioengineering, University of Texas at Dallas, Dallas, TX 75080

[4]Advanced Light Source, Lawrence Berkeley National Laboratory, Berkeley, CA 94720

*both authors contributed equally, and are first authors

[#]corresponding author

Sunita P. Ho, Ph.D.

Division of Preclinical Education, Biomaterials and Engineering

Department of Preventive and Restorative Dental Sciences, D 3210

700 Parnassus Avenue, School of Dentistry

University of California San Francisco

San Francisco, CA 94143

Phone: 415-514-2818

email: sunita.ho@ucsf.edu

ABSTRACT

Spatiotemporal implant-bone biomechanics and mechanoadaptive strains in peri-implant tissue are poorly understood. Physical and chemical characteristics of an implant-bone complex (IBC) were correlated in three-dimensional space (along the length and around a dental implant) to gather insights into time related integration of the implant with the cortical portion of jaw bone in a rat. Rats (N = 9) were divided into three experimental groups with three rats per time point 3-, 11-, and 24-day. All rats were fed crumbled hard pellets mixed with water (soft-food diet) for the first 3 days followed by a hard-food diet with intact hard-food pellets (groups of 11- and 24-day only).

Biomechanics of the IBCs harvested from rats at each time point was evaluated by performing mechanical testing *in situ* in tandem with X-ray imaging. The effect of physical association (contact area) of a loaded implant with adapting peri-implant tissue, and resulting strain within was mapped by using digital volume correlation (DVC) technique. The stiffness of the IBC at respective time points was correlated with mechanical strain in bone. Results illustrated that the stiffness of the IBC at 11-day was lower than that observed at 3-day. However, at 24-day, IBC stiffness recovered to that which was observed at 3-day. Correlative microscopy and spectroscopy illustrated that the lower IBC stiffness was constituted by softer and less mineralized peri-implant tissue that contained varying expressions of osteoconductive elements. Lower stiffness observed at 11-day was constituted by less mineralized peri-implant tissue with osteoconductive elements that included phosphorus (P) which was co-localized with higher expression of zinc (Zn), and lower expression of calcium (Ca). Higher stiffness at 24-day was constituted by mineralized peri-implant tissue with higher expressions of osteoconductive elements including Ca and P, and lower expressions of Zn. These spatiotemporal correlative maps of peri-implant tissue architecture, heterogeneous distribution of mineral density, and elemental colocalization underscore mechanoadaptive

physicochemical properties of peri-implant tissue that facilitate functional osseointegration of an implant. These results provided insights into **1)** plausible “prescription” of mechanical loads as an osteoinductive “therapeutic dose” to encourage osteoconductive elements in the IBC that would facilitate functional osseointegration of the implant; **2)** a “critical temporal window” between 3 to 11 days, and perhaps it is this acute phase during which key candidate regenerative molecules can be harnessed to accelerate osseointegration of an implant under load.

Keywords: Implant-bone complex (IBC), spatiotemporal biomechanics, implant function, bone remodeling, functional osseointegration, X-ray fluorescence microprobe

1. INTRODUCTION

The primary and intended function of an implant-bone complex (IBC) is to sustain cyclic chewing loads of varying magnitudes and frequencies (dependent on food hardness) throughout the lifespan of a human. The two structural components that constitute an IBC are, the dental implant, usually made out of a metal, and the mechanoresponsive bone in which the implant is placed. Of the two components, from a materials and mechanics perspectives, implants are mechanically tested to identify modes of implant failure resulting from cyclic loads prior to their release into the market. However, biological assessments of an implant at a cell- and tissue-level should not be the only measure of implant biocompatibility. Current available methods to measure implant stability and estimate functional “durability” include, the force needed to push, pull, and torque the implant from bone at varying loading frequencies [1, 2]. Despite these guidelines, dental implants fail as a result of multiple “stressors” that include, bacteria, corrosion, extraneous loads, and impaired bone quality. The causation of each said effector/stressor in and of itself is a challenge to determine failure of an IBC. This multivariate challenge to predict IBC failure risk becomes monumental when investigated within the context of dynamic function on the IBC and mechanoadaptation of peri-implant tissue including bone.

Bone is a mechanoadaptive tissue, and the adaptive response is to sustain both static and dynamic developmental and growth related functional demands [3-5]. However, mechanoadaptive response of bone and resulting bone quality in the context of IBC function, and IBC risk to failure is minimally investigated and understood. More recently, mechanobiological processes within bone [5] and peri-implant tissue of an IBC [6] were mapped using rat models. Spatial and temporal correlation of physical and mechanical characteristics of an IBC to the mechanoadaptive markers, such as the

osteoinductive and osteoconductive markers of the peri-implant tissue are yet to be understood. As such, the time-sensitive windows of mechanical strain (osteoinductive) induced biochemical and elemental expressions (osteoconductive) that could be harnessed to accelerate implant integration with bone through regenerative methods are missed, and are left unquestioned and uninvestigated [7]. Instead, IBC continues to be investigated exhaustively for its chemical characteristics, mostly osteoconductive stimuli, using materials science approach with minimal to no reference to function [8-14]. Materials science approach involves the use of multiscale imaging through several microscopy and spectroscopy methods. These methods undoubtedly illustrate chemical characteristics of the implant-bone interface at various length-scales including cell- and tissue-levels, but do not consider how these levels scale with the IBC as a whole, in particular, a loaded IBC. In other words, the characteristics of the implant-bone interface and failure detection using simulated loads are minimally investigated in the greater context of IBC biomechanics.

IBC biomechanics constitutes three main entities, the implant, bone and the implant-bone interface including associated soft tissues. As such, IBC biomechanics is equally important as cell and tissue-level implant biocompatibility tests. This multiscale characterization of an IBC would permit scaling between cells, tissues and the entire complex within the context of mechanoresponsive and ensuing spatiotemporal adaptive nature of the IBC. In this study, a hybrid method, a combination of functional imaging and correlative microscopy and spectroscopy is used to visualize and investigate functional significance [15, 16] of adapting peri-implant tissues within intact IBCs. *In silico* modeling techniques including finite element methods [6] are often used to estimate tissue mechanics and infer functional significance of IBC [17]. Other experimental mechanics techniques such as photoelastic, Moiré and electron-speckled pattern interferometry are performed on “sectioned” specimens [18, 19].

Functional imaging, however, is a combination of biomechanical testing of “intact” specimens using X-rays, and a post analyses of mechanical strains within peri-implant tissues using digital volume correlation (DVC) technique. Functional imaging, in this study is performed by loading the IBC using a mechanical testing device coupled to a micro X-ray computed tomography (micro XCT) system. As such, the physical association of the implant with the peri-implant tissue at no load correlated with that observed under loaded conditions will be used to localize strains and strain discontinuities within peri-implant tissues at different time points.

The correlation of physical and chemical characteristics of craniofacial cortical bone adjacent to the implant in three-dimensional (3D) space and time will provide insights into functional osseointegration of the implant. Spatiotemporal correlation between physical (osteoinductive) and chemical characteristics (osteoconductive) in the context of mechanoadaptation will be illustrated by using the hybrid method on several IBCs harvested from rats. Spatiotemporal expressions of osteoinductive and osteoconductive markers indicating mechanoadaptation of IBC will be mapped in four steps. **(1)** Image IBC under load using X-rays to evaluate **a)** stiffness and failure point of IBCs from load-displacement curves, and **b)** implant-bone contact area, bone volume fraction, and bone mineral density from implant-bone physical association as observed in digitally collected X-ray scans; **(2)** digitally correlate volumes of IBC under load and unloaded conditions to map compressive/tensile strains, and shifts in maximum and minimum principal strains within the peri-implant tissue**;** and **(3)** use X-ray fluorescence microprobe to identify calcium (Ca), phosphorus (P), zinc (Zn), and titanium (Ti) elements to analyze the spatial distribution and co-localization of elements within peri-implant tissue. Finally, **(4)** correlate spatiotemporal changes of these osteoinductive (physical parameters including shifts in mechanical strains) and osteoconductive (elements and their co-localization

properties of an IBC) markers in the peri-implant tissue. Insights into mechanoadaptive nature of the peri-implant tissue, and osseointegration of implants and their functional durability will be discussed within the context of immediate and delayed function through modulation of food hardness.

2. MATERIALS AND METHODS

2.1 Sample preparation

All animal experiments conducted in this study were housed in pathogen-free conditions in compliance with the guidelines of the Institutional Animal Care and Use Committee (IACUC) of University of Texas at Dallas and the National Institutes of Health (NIH). Nine male Lewis rats (10 weeks old, 320 g of weight on average) were obtained from Charles River (Wilmington, MA, USA). Titanium implant screws of 2 mm in diameter, and 76 mm in length, were placed in the edentulous maxillary alveolar crest of each rat (**figure 1**). Dental implantation surgery was conducted at University of Texas at Dallas and was similar to that which was previously described [20, 21]. All rats were weighed before and after surgery, and were monitored daily for eating and grooming. After the surgical procedure, rats were divided into three experimental groups with three time points (N = 3): 3-, 11-, and 24-day. After implantation surgery, the rats were fed crumbled hard pellets mixed with water (soft-food diet) for the first 3 days with sterile water *ad libitum* (all groups), followed by a hard-food diet with intact hard-food pellets (groups of 11- and 24-day only). At each designated time point (3-, 11-, and 24-day after Ti-screw implantation), each rat was euthanized with an excessive dose of sodium pentobarbital and the collected maxillae were snap frozen in 1X phosphate buffered saline and were stored at -80 ^{o}C.

2.2 Compression test *in situ*

Compression tests on IBCs were performed *in situ* using a tension/compression stage (MT10352,

500N Nano Tomography, Deben UK Limited, West Sussex, UK) coupled to a micro X-ray computed tomography system (MicroXCT-200, Carl Zeiss X-ray Microscopy, Pleasanton, CA, USA) (**figure 2**). For biomechanical tests, the IBCs were cut into cubes of ~5×5×4 mm^3 from the jaw bones of rats. All specimens were vertically orientated so that the loading axis was aligned with the implant longitudinal axis, thereby avoiding eccentric loads. Polymethylmethacrylate (PMMA) resin was used to support and immobilize the specimens on the loading stage. Dental composite was mounted on top of the implant and was cured with a dental curing light. The composite buildup was trimmed to create a flat surface parallel to the loading anvil using a dental hand piece (Marathon Electric Micromotor Polishing Unit 35K RPM Handpiece) for uniform loading.

The specimens from all three time points were compressed at a loading rate of 0.2 mm/min until the IBC failure was registered as a sudden drop in load in the reactionary force and displacement curve. From the reactionary force and displacement curve, the IBC stiffness was calculated as the slope of the reactionary force-displacement curve (**figure 2**). X-ray tomograms (spatial resolution: ~4.16 mm/voxel, X-ray source energy: 90 kV, magnification: 4X) were collected at the unloaded stage and after failure. A stepwise compression test was conducted on 3-day IBC using the same experimental devices and setup. The IBC was loaded to 4 N, 8 N, 12 N, and subsequently to failure at a loading rate of 0.2 mm/min to evaluate and map the shifts in maximum and minimum principal strains within the peri-implant tissue. After loading to a peak force of 4 N, 8 N, 12 N and to failure respectively, a 5-min wait period was set prior to CT imaging to allow the respective loads to equilibrate. Tomograms were reconstructed following which segmentation was performed to determine a) peri-implant tissue contact area with bone, b) bone mineral density, and c) bone-volume fraction using AVIZO software (FEI Visualization Sciences Group, Burlington, MA, USA).

2.3 Strain mapping of an IBC

Digital volume correlation (DVC) was performed to map strain localization within the peri-implant tissue by correlating the voxels of the IBC under loaded and unloaded conditions. For strain calculation, one specimen from each time point was selected. The region of interest (ROI) was selected as a domain with a size of ~250×250×140 voxel^3 (physical size: 1.04×1.04×0.58 mm^3) surrounding the dental implant. During DVC, calculation points were evenly distributed within bone at a grid step of 2 voxels, and sub-volume size was chosen as 41×41×41 voxel^3 (physical size: 0.17×0.17×0.17 mm^3) at each calculation point. Finally, maximum/minimum principal strains within the bone adjacent to the interface of the IBC were evaluated. Maximum/minimum principal strains are defined as the extreme normal strains at a point occurring in the plane where shear strains are zero (in a theoretical sense). All DVC analyses were implemented using a software written in C++ language as previously described [22].

2.4 Elemental mapping

The specimens were imaged using micro XCT at 4X magnification (~5 μm/pixel) and 50kVp of energy. Following micro XCT, the specimens were embedded in epoxy resin and hemi-sectioned using a slow speed saw. The cut surfaces were ground down to a fine roughness using silicon carbide grit paper and subsequently mirror-finished using a series of diamond suspension slurries that included 6, 3, 2, 1 and 0.5 μm. Micro-focused X-ray fluorescence elemental distribution maps of calcium (Ca), phosphorus (P), and zinc (Zn) from sectioned specimens at 3- and 11-day were collected using X-ray fluorescence microprobe (XRF microprobe) at beamline 10.3.2 of Advanced Light Source (ALS) at Lawrence Berkeley National Laboratory (LBNL) [23]. Spatial maps of elemental counts were generated using an incident energy beam of 10 keV, and a spot size of ~5×5 μm.

The relative grey scale differences in arbitrary units (a.u.) from X-ray tomograms were used to map relative differences in mineral density. Additionally, multiple micro XCT slices were selected and averaged to account for the microprobe XRF penetration depth for accurate spatial correlation of mineral density and elemental maps obtained from the same specimen. The averaged micro XCT tomograms were adjusted to register with the microprobe XRF elemental maps using AVIZO. Ca, P, and Zn maps were segmented into Ca-, P-, and Zn-enriched regions based on a threshold of mean plus standard deviation. MD analysis within the region was performed after extracting MD maps corresponding to Ca-, P-, and Zn-enriched spatial coordinates. Additional elemental analyses were performed using an energy dispersive X-ray mode (Quantax EDS, Bruker Nano Inc., Madison, WI, USA) to collect elemental maps and spectra of carbon (C), Ca, P, and Ti at 18 keV using a variable pressure chamber.

2.5 Statistical Analysis

Statistical analysis using Mann–Whitney U test / Wilcoxon rank-sum test was used to test for pairwise (3-day vs. 11-day, 11-day vs. 24-day, 3-day vs. 24-day) statistical differences in joint stiffness and failure load between time groups (3-, 11-, and 24-day). P-value < 0.05 was considered to be statistically significant. Mann-Whitney U test was preferred over other parametric tests given the number of specimens per group ($N = 3$), and the sampling of each specimen within a group, and normality assumptions (histograms illustrating data distribution) with parametric (for e.g., t-test, Z-test, ANOVA) tests. Differences in normalized grayscale of bone and soft-tissue, and maximum and minimum principal strain were tested using analysis of variance (ANOVA) followed by post hoc multiple comparison adjusted t-tests (Holm–Šidak, unpaired, two-tails). Parametric tests are justified

to identify mineral density differences between groups because of the vast sampling density per specimen and per group.

3. RESULTS

3.1 Biomechanics of an Implant-Bone Complex (IBC)

The reactionary force-displacement curves obtained from the biomechanical testing of the IBCs are illustrated in figure 2. The stiffness and load-to-failure of the 11-day group decreased from 3-day group. However, the stiffness and load-to-failure of the 24-day group were higher than the 11-day group and when compared to the 3-day group. Variability in stiffness and load-to-failure of the 11-day and 24-day groups were observed when compared to 3-day group. The stiffness (mean value ± standard deviation) of the IBC decreased from 98±13 N/mm (3-day group, red) to 51±23 N/mm (11-day group, blue), and increased to 123±38 N/mm (24-day group, yellow). The load-to-failure of IBC followed the same trend as the stiffness; it decreased from 15±2 N at 3-day to 9±3 N at 11-day group, and increased to 16±3 N at 24-day. No significant differences ($p > 0.05$) in IBC stiffness values and failure loads across time points were observed due to a sample size of $N = 3$.

3.2 Mineral Density of the Peri-Implant Tissue

The rendered volumes of IBCs in all experimental groups display relative location of the implant with respect to the peri-implant tissue (**figures 3 and 4**). 2D tomograms of the IBCs illustrate implant location relative to peri-implant tissue. In the 2D virtual section of the 11-day IBC, darker grey regions are predominantly organic, while lighter grey are predominantly inorganic regions. Specifically, the grayscale of dental implants was approximately 65535, and that of the predominantly inorganic peri-implant tissue was 35000 to 50000 (53% to 76% of implant), while the grayscale of predominantly organic peri-implant tissue varied from 25000 to 35000 (38% to 53% of implant). In comparison to the

3-day group and 24-day group, less mineralized peri-implant tissue was observed in the 11-day group. Specifically, the volume fraction of the peri-implant tissue within the ROI decreased from 43% at 3-day to 33% at 11-day, and increased to 53% at the 24-day group. Regions not affected by X-ray beam hardening were chosen to analyze intensity-based differences in the IBC.

3.3 Contact Area of the Peri-Implant Tissue with an Implant

In experimental groups illustrated similar contact areas of the peri-implant tissue. At 3-day, the contact area was 3.14 mm^2, at 11-day it was 2.99 mm^2, and at 24-day it was 3.15 mm^2. However, the 11-day group displayed much less contact area between predominantly inorganic peri-implant tissue and implant than that which was observed in other two groups (**figure 3**), indicating the temporal variations in peri-implant tissue and implant contact. The mineralized peri-implant tissue-implant contact ratio was 14.0%, 1.6%, and 30.4% in the 3-, 11-, and 24-day groups, respectively. Consequently, the contact area decreased from 0.44 mm^2 at 3-day group to 0.05 mm^2 in 11-day group, and increased to 0.96 mm^2 in 24-day group. The trend of temporal variation of contact area between peri-implant tissue and implant is in contrast with that of the temporal variation of average surface distance between mineralized bone and implant. The mineralized implant-bone distance at 3-day was 32 μm and increased to 126 μm at 11-day. However, it decreased at 24-day to a value of 41 μm (**figure S1**).

3.4 Strain Responses in Peri-Implant Tissue of an IBC

The maximum and minimum principal strain maps within the mineralized bone tissue and the organic construct (less mineralized bone tissue) after the failure of IBC in three groups are illustrated in figure 3. It is worth to note that the 11-day group illustrated higher contact area than the other two groups as the organic construct also was included as a part of the peri-implant tissue. The maximum

principal strain (tensile) was mostly concentrated in the predominantly inorganic or highly X-ray attenuating regions of the peri-implant tissue that is in contact with the crestal regions of Ti threads, while the minimal principal strain (compressive) is mostly distributed in the peri-implant tissue adjacent to the shank region of the screw/implant. Moreover, the minimal principal strain in the 11-day group illustrated a higher value on average (**figure 3**) and the strain was spread over a large contact area (**figure 3**) compared with the 3-day group and 24-day group ($p < 0.05$). To be specific, the average maximum (minimum) principal strain levels within the ROI in the 3-, 11-, and 24-day groups were maximum tensile strain of 8.3% (minimum compressive strain of -9.8%), 10.0% (-15.8%) and 8.6% (-8.4%), respectively ($p < 0.05$). Statistically significant ($p < 0.05$) difference between maximum principal strain and minimum principal strain in the peri-implant tissue at each time point and across different time points was observed (**figure 3**). **Stepwise Strain Responses in Peri-Implant Tissue of an IBC (see figure S2):** The maximum and minimum principal strain maps within the craniofacial cortical bone under stepwise compression of the IBC in the 3-day group are illustrated in figure S2. As the compressive load increased, both maximum and minimum principal strains within the ROI increased. However, the higher-level strains were spread in peri-implant tissue surrounding the Ti threads. Consequently, the accumulation of local bone damage induced variations in principal strain patterns and the global failure of the IBC occurred in the last incremental load (**figure S2**).

3.5 Elemental Composition of the Peri-Implant Tissue in an IBC

The heterogeneous elemental composition of bone near the implant-bone interface is shown in figure 4. Elemental composition is correlated with mineral density within peri-implant tissue. Softer tissue matrix next to the implant grooves and mineralized matrix farther away from the grooves can be observed. Distributions of Ca and P were homogenous within the surrounding peri-implant tissue.

Zn was concentrated in both soft and hard tissue surrounding the implant predominantly in peri-implant tissue at 11-day. Zn, however, was higher in lower density region lower counts of Ca and P. Zn was lower in higher mineral density region with higher counts of Ca and P (**figures 4, S3, S4**).

4. DISCUSSION

In this study, a hybrid method, a combination of functional imaging and correlative microscopy and spectroscopy was used to visualize and investigate functional significance, and thereby gather insights into mechanoadaptation of peri-implant tissue. Functional imaging, allowed us to visualize the effect of the physical properties of an implant, the bone, and the implant-bone interface including the surrounding softer tissues on simulated function. Function of an IBC, in general, is its capacity to sustain cyclic loads (magnitude, frequency-dependent, and duration) resulting from chewing. Several primary and secondary factors contribute to the mechanical integrity of an IBC. The primary factors that control functional osseointegration of an implant include, original bone quality at the time of implantation, implant design/form, and physical relationship of an implant with the peri-implant tissue [24]. These factors guide load distribution and mechanical strain within the peri-implant tissue and consequently its temporal mechanoadaptation. Following implantation, in this study, mineral density of peri-implant tissue varied with time (**figure 3**). At 3-day, the mechanical interlock of the implant with bone with a contact ratio of 14% was a key factor that contributed to IBC stiffness and its load to failure. However, extending the healing through additional 8 days, illustrated plausible osteoclast-dominated remodeling; an inevitable acute response to implantation [25]. Consequently, the bone volume fraction decreased from 43% in the 3-day group to 33% in the 11-day group (**figure 3**), and the implant-bone contact ratio reduced from 14.0% at 3-day compared to 1.6% at 11-day. However, at 11-day time point, an increase in percent contact of the implant with organic matrix (semi-

radiotransparent organic matrix in contrast with radiopaque bone) (**figure 3**, **movie S1**, **figure S1**) resulted in an increased “plastic” zone as was evident from the load-displacement curve in addition to a decreased IBC stiffness (51±23 N/mm). Interestingly, the organic dominant peri-implant tissue demonstrated a maximum shift between compressive and tensile strains in response to compressive load (**figure 2**). Mineral formation in the peri-implant tissue occurred for additional 13 days. The increased mineralization of the peri-implant tissue resulted in a decreased shift between compressive and tensile strains, and increased IBC stiffness (123±38 N/mm) and load-to-failure (16±3 N) (**figure 2**). Furthermore, the continued mineral formation in the peri-implant organic tissue was in agreement with increased contact between mineralizing peri-implant tissue and the implant (contact ratio: 30.4%) and bone volume fraction (53%).

To ensure functional osseointegration, functional loads should facilitate physiologic remodeling with a balance between blastic and clastic activities of cells stimulated by “osteoinductive shifts”, that are shifts in strain gradients in peri-implant tissue. In this study, 3 to 11 days was identified as a “temporal window” that allowed us to gather insights into strains and mechanoadaptation of peri-implant tissue. Data illustrated that the organic polymeric fabric blanketing a dental implant, could, to an extent mimic periodontal ligament load-absorbing and –bearing characteristics. More importantly, modulation of this organic fabric with a “mechanical dose” (dose is dependent on magnitude, frequency and duration at which it is applied) could accelerate regeneration and integration of a mineralized matrix similar in its biomechanical performance as that of a tooth ankylosed to bone [26-28]. It is proposed that this window of opportunity should be exploited to maximize the “biomechanical gains” for an IBC.

Results are a manifestation of biomechanical and multiple mechanobiological pathways in the

IBC over space (length of the implant) and time. In our experimental model, direct function mediated strain in bone is minimal. This is because of the anatomical location of the implant at a site farther away from the sites of the three molars commonly used for chewing. However, the implant was placed in a region with biomechanical advantage, between the incisors and the first molars; a region that is subjected to mechanical strains resulting from gnawing (incisors) and chewing (molars). Given this scenario, continued access to hard pellet food with a higher stiffness value compared to soft chow [29] could have resulted in mechanical stimuli and shifts in strain equivalent to food hardness. These shifts are presumed “stressors/effectors” that promote expression of osteogenic proteins and/or differentiation of cells into an osteogenic lineage in the peri-implant tissue.

An osteoconductive marker for mineralization is colocalization of Zn with Ca and P. Zn was observed in the peri-implant tissue, but at a higher level in peri-implant tissue with lower mineral density compared to lower Zn levels in a higher mineral density tissue (**figures 4, S3, and S4**). Additionally, higher levels of Zn were also observed in softer matrices by correlating electron micrographs with X-ray fluorescence elemental maps (**figures 4, S3 and S4**). Relative expressions of Zn continue to be reported in multiple soft tissues, including the periodontal ligament [30], cartilage [31], and more mineralized tissues including bone, dentin and cementum [32] in humans. The presence and localization of Zn, however, was described to be site-specific and continues to be discussed under both sterile and nonsterile conditions and exacerbated pathological loading conditions [30, 32, 33]. Zn in particular is associated with calcium based apatite $(Ca_{10-x}Y_x)(PO_4)_6(OH)_{2-p}(CO_3)_p$, where Y represents trace metals that could include Zn, Mg and Sr [34, 35]. Within the context of mineralizing peri-implant tissue, it is proposed that, presence of Zn in association with P could be linked to three parallel or serially occurring scenarios: 1) biomineralization through

pyrophosphate (PPi) and phosphate (Pi) (PPi-Pi) axis [36] that is facilitated by tissue nonspecific alkaline phosphatase whose function is permitted by Zn; 2) inflammation-mediated wound healing pathway through matrix metalloproteinases whose function also is mediated by Zn [37]; 3) presence of osteogenic cells with expression of zinc-finger proteins such as osterix [38]. Of the three elements localized in this study, Zn in particular, has been demonstrated to be an osteoconductive element [39-42]. Its presence is likely under osteoinductive conditions, mechanical loads included. The presence of Zn in the peri-implant tissue should be leveraged to accelerate healing of the implantation site, while facilitating an effective integration with the implant [43, 44]. Therefore, it is proposed that immediate, but intermittent loading could accelerate implant integration. Intermittent loading would facilitate significant shifts between compressive and tensile strains in the peri-implant tissue (osteoinductive) (**figure 3, figure 5, figure S2**). However, the failure load of the IBC a few days following implantation also decreased indicating an increased risk to failure specifically when chewing on harder foods. Food hardness, as such should be appropriately regulated to ensure functional load lower than the failure load, as the load-to-failure of the IBC is significantly lower in this time window. Additionally, it should be noted that differences in bone biology might exist between species and between dissimilar bones within the same species **Error! Reference source not found.**. The “window o f opportunity” for mechanical stimulation, therefore could be species- and sex-dependent, bone-type and bone quality, all of which can affect functional osseointegration of dental and orthopedic implants.

5. CONCLUSIONS

This study highlights the importance of a hybrid method, a combination of functional imaging, and correlative microscopy and spectroscopy. The method enables visualization of mechanoadaptive nature of peri-implant tissue, and there by, the functional significance of an IBC.

Limitations of the study include, **1)** a loss of information by virtue of the resolution mismatch between microscopy and spectroscopy methods used in this work. An ideal scenario would permit a) localization of cell type affected b) by a shift in mechanical strain (osteoinductive) through c) colocalization of the presence of osteogenic proteins and elements (osteoconductive) that would help explain d) functional biomechanics of an IBC; **2)** spatiotemporal differences in IBC biomechanics is limited to trends. Future studies should be performed on larger specimen population to map significant differences in spatiotemporal mechanoadaptive nature of the IBC in rats. Regardless, biomechanical testing *in situ* coupled with X-ray CT imaging allowed us to illustrate spatiotemporal mechanoadaptation of peri-implant tissue spatial and temporal windows have enabled visualization of the effect of physical (contact area, load-to-failure, maximum tensile strain, maximum compressive strain, bone volume) and chemical (mineral density of peri-implant tissue, element composition) characteristics of peri-implant tissue on the functional quality of an IBC in rats. This proof-of-concept study provided insights that include, 1) “prescription” of mechanical loads as an osteoinductive “therapeutic dose” to encourage osteoconductive elements in the IBC that would facilitate functional osseointegration of the implant; 2) a “critical temporal window”, perhaps the acute phase during which key candidate regenerative molecules can be harnessed to accelerate osseointegration of an implant under load.

Contributions from the authors

S.P.H. conception of the study, design of experiments, data analyses and interpretation, critically revised the manuscript; S.P.H. and D.C.R. provided funding; B.W. and K.K. conducted experiments and performed data analyses and composed the first draft of this manuscript; D.C.R. provided specimens and feedback on the manuscript, S.E.W. worked on the animal model,

harvested specimens and feedback on the manuscript, B.W., K.K., and M.K. performed micro-CT and pertinent data analyses; S.S. performed statistical data analyses; P.U. performed data analyses with S.S. and edited manuscript with D.C.R., B.W., and K.K.; M.K. and S.F. performed microprobe XRF at Advanced Light Source, Lawrence Berkeley National Laboratories.

Acknowledgements

The authors would like to thank Ms. Grace Nonomura for her help in specimen preparation. The authors thank the Biomaterials and Bioengineering Correlative Microscopy Core (http://bbcmc.ucsf.edu), UCSF for the use of their MicroXCT-200 and SIGMA 500-VP Field Emission Electron Microscope – Scanning and Transmission. This research used beamline 10.3.2 of the Advanced Light Source, a DOE Office of Science User Facility under contract no. DE-AC02-05CH11231.

Funding: This work was supported by the National institutes of Health, NIDCR R01 DE022032 (SPH), NIDCR R21 DE027138 (SPH), NIDCR R01 DE026736 (DCR) and by Delta Dental Community Care Foundation (KK).

REFERENCES

[1] Swami V, Vijayaraghavan V, Swami V. Current trends to measure implant stability. Journal of Indian Prosthodontic Society. 2016;16:124-30.

[2] Boronat Lopez A, Balaguer Martinez J, Lamas Pelayo J, Carrillo Garcia C, Penarrocha Diago M. Resonance frequency analysis of dental implant stability during the healing period. Medicina oral, patologia oral y cirugia bucal. 2008;13:E244-7.

[3] Carter DR. Mechanobiology in rehabilitation science. Journal of rehabilitation research and development. 2000;37:vii-viii.

[4] Carter DR, Beaupre GS. Skeletal function and form: mechanobiology of skeletal development, aging, and regeneration: Cambridge, U. K.; 2001.

[5] Carter DR, Beaupre GS, Giori NJ, Helms JA. Mechanobiology of skeletal regeneration. Clinical orthopaedics and related research. 1998:S41-55.

[6] Li J, Yin X, Huang L, Mouraret S, Brunski JB, Cordova L, et al. Relationships among Bone Quality, Implant Osseointegration, and Wnt Signaling. Journal of dental research. 2017;96:822-31.

[7] Albrektsson T, Johansson C. Osteoinduction, osteoconduction and osseointegration. European spine journal : official publication of the European Spine Society, the European Spinal Deformity Society, and the European Section of the Cervical Spine Research Society. 2001;10 Suppl 2:S96-101.

[8] Alvarez K, Fukuda M, Yamamoto O. Titanium Implants after alkali heating treatment with a [Zn(OH)4]2 complex: analysis of interfacial bond strength using push-out tests. Clinical implant dentistry and related research. 2010;12 Suppl 1:e114-25.

[9] Chang YY, Lai CH, Hsu JT, Tang CH, Liao WC, Huang HL. Antibacterial properties and human gingival fibroblast cell compatibility of TiO2/Ag compound coatings and ZnO films on titanium-based material. Clinical oral investigations. 2012;16:95-100.

[10] Feng W, Zhao BH, Zhang W, Lin Z. [An experimental study of Zn/Ca/P-containing coatings on titanium implant surface modified by plasma electrolytic oxidation]. Zhonghua kou qiang yi xue za zhi = Zhonghua kouqiang yixue zazhi = Chinese journal of stomatology. 2019;54:46-51.

[11] Li Q, Li L, Zhao M, Dong L, Wu J, Li D. Biological actions of Cu/Zn coimplanted TiN on Ti-6Al-4V alloy. Biointerphases. 2019;14:051008.

[12] Mistry S, Roy S, Jyoti Maitra N, Roy R, Datta S, Chanda A, et al. Safety and efficacy of additive and subtractive surface modification of Ti6Al4V endosseous implant in goat bone. Journal of the mechanical behavior of biomedical materials. 2016;57:69-87.

[13] Roguska A, Belcarz A, Zalewska J, Holdynski M, Andrzejczuk M, Pisarek M, et al. Metal TiO2 Nanotube Layers for the Treatment of Dental Implant Infections. ACS applied materials & interfaces. 2018;10:17089-99.

[14] Zhu C, Lv Y, Qian C, Ding Z, Jiao T, Gu X, et al. Microstructures, mechanical, and biological properties of a novel Ti-6V-4V/zinc surface nanocomposite prepared by friction stir processing. International journal of nanomedicine. 2018;13:1881-98.

[15] Du J, Lee JH, Jang AT, Gu A, Hossaini-Zadeh M, Prevost R, et al. Biomechanics and strain mapping in bone as related to immediately-loaded dental implants. Journal of biomechanics.

2015;48:3486-94.

[16] Jang AT, Lin JD, Seo Y, Etchin S, Merkle A, Fahey K, et al. In situ compressive loading and correlative noninvasive imaging of the bone-periodontal ligament-tooth fibrous joint. Journal of visualized experiments : JoVE. 2014.

[17] Huang L, Liu B, Cha JY, Yuan G, Kelly M, Singh G, et al. Mechanoresponsive Properties of the Periodontal Ligament. Journal of dental research. 2016;95:467-75.

[18] Wang RZ, Weiner S. Strain-structure relations in human teeth using Moire fringes. Journal of biomechanics. 1998;31:135-41.

[19] Zaslansky P, Friesem AA, Weiner S. Structure and mechanical properties of the soft zone separating bulk dentin and enamel in crowns of human teeth: insight into tooth function. Journal of structural biology. 2006;153:188-99.

[20] Mouraret S, Hunter DJ, Bardet C, Brunski JB, Bouchard P, Helms JA. A pre-clinical murine model of oral implant osseointegration. Bone. 2014;58:177-84.

[21] Biguetti CC, Cavalla F, Silveira EM, Fonseca AC, Vieira AE, Tabanez AP, et al. Oral implant osseointegration model in C57Bl/6 mice: microtomographic, histological, histomorphometric and molecular characterization. Journal of applied oral science : revista FOB. 2018;26:e20170601.

[22] Wang B, Pan B. Self-Adaptive Digital Volume Correlation for Unknown Deformatoin Fields. Experimental Mechanics. 2018;59.

[23] Marcus MA, MacDowell AA, Celestre R, Manceau A, Miller T, Padmore HA, et al. Beamline 10.3.2 at ALS: a hard X-ray microprobe for environmental and materials sciences. Journal of synchrotron radiation. 2004;11:239-47.

[24] Brunski JB. Biomechanical factors affecting the bone-dental implant interface. Clinical materials. 1992;10:153-201.

[25] Roberts WE, Huja S, Roberts JA. Bone modeling: biomechanics, molecular mechanisms, and clinical perspectives. Seminars in orthodontics. 2004;10:123-61.

[26] Roberts WE. Bone dynamics of osseointegration, ankylosis, and tooth movement. Journal. 1999;78:24-32.

[27] Roberts WE, Epker BN, Burr DB, Hartsfield JK, Roberts JA. Remodeling of mineralize tissues, Part II: Control and Pathophysiology. Seminars in orthodontics. 2006;12:238-53.

[28] Roberts WE, Garetto LP, DeCastro RA. Remodeling of devitalized bone threatens periosteal margin integrity of endosseous titanium implants with threaded or smooth surfaces: indications for provisional loading and axially directed occlusion. Journal. 1989;68:19-24.

[29] Niver EL, Leong N, Greene J, Curtis D, Ryder MI, Ho SP. Reduced functional loads alter the physical characteristics of the bone-periodontal ligament-cementum complex. Journal of periodontal research. 2011;46:730-41.

[30] Grandfield K, Herber RP, Chen L, Djomehri S, Tam C, Lee JH, et al. Strain-guided mineralization in the bone-PDL-cementum complex of a rat periodontium. Bone reports. 2015;3:20-31.

[31] Kraus VB. Osteoarthritis: The zinc link. Nature. 2014;507:441-2.

[32] Djomehri SI, Candell S, Case T, Browning A, Marshall GW, Yun W, et al. Mineral density volume

gradients in normal and diseased human tissues. PloS one. 2015;10:e0121611.

[33] Ho SP, Kurylo MP, Grandfield K, Hurng J, Herber RP, Ryder MI, et al. The plastic nature of the human bone-periodontal ligament-tooth fibrous joint. Bone. 2013;57:455-67.

[34] Bhattacharya PT, Misra SR, Hussain M. Nutritional Aspects of Essential Trace Elements in Oral Health and Disease: An Extensive Review. Scientifica. 2016;2016:5464373.

[35] Procopio A, Malucelli E, Pacureanu A, Cappadone C, Farruggia G, Sargenti A, et al. Correction to Chemical Fingerprint of Zn-Hydroxyapatite in the Early Stages of Osteogenic Differentiation. ACS central science. 2019;5:1731.

[36] Russell RG, Fleisch H. Pyrophosphate and diphosphonates in skeletal metabolism. Physiological, clinical and therapeutic aspects. Clinical orthopaedics and related research. 1975:241-63.

[37] Kim JH, Jeon J, Shin M, Won Y, Lee M, Kwak JS, et al. Regulation of the catabolic cascade in osteoarthritis by the zinc-ZIP8-MTF1 axis. Cell. 2014;156:730-43.

[38] Ganss B, Jheon A. Zinc finger transcription factors in skeletal development. Critical reviews in oral biology and medicine : an official publication of the American Association of Oral Biologists. 2004;15:282-97.

[39] Barron M, Franklin L, Woodall J, Jr., Wingerter S, Benghuzzi H, Tucci M. Comparison of osteoconductive materials on MG63 osteoblast cell function. Biomedical sciences instrumentation. 2007;43:248-53.

[40] Cai YD, Wang SM, Chou AH, Yu LY, Sun J. Zinc-coated carbonate apatite derived from avian eggshell for potential use as bone substitute. Part I: preparation and properties. Implant dentistry. 2012;21:230-5.

[41] Pina S, Vieira SI, Rego P, Torres PM, da Cruz e Silva OA, da Cruz e Silva EF, et al. Biological responses of brushite-forming Zn- and ZnSr- substituted beta-tricalcium phosphate bone cements. European cells & materials. 2010;20:162-77.

[42] Snead D, Barre P, Bajpai PK, Taylor A, Reynolds D, Mehling B, et al. The use of a zinc based bioceramic as an osteoconductive agent in the rat model. Biomedical sciences instrumentation. 1995;31:141-6.

[43] Pavlin D, Dove SB, Zadro R, Gluhak-Heinrich J. Mechanical loading stimulates differentiation of periodontal osteoblasts in a mouse osteoinduction model: effect on type I collagen and alkaline phosphatase genes. Calcified tissue international. 2000;67:163-72.

[44] Pavlin D, Gluhak-Heinrich J. Effect of mechanical loading on periodontal cells. Critical reviews in oral biology and medicine : an official publication of the American Association of Oral Biologists. 2001;12:414-24.

Figure 1

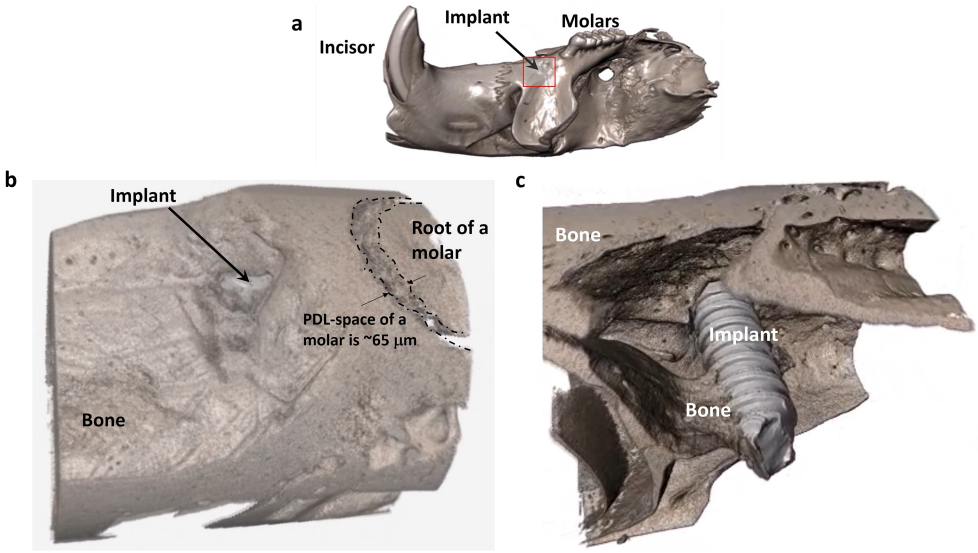
a
Incisor
Implant
Molars
b
Implant
Root of a molar
PDL-space of a molar is ~65 µm
Bone
c
Bone
Implant
Bone

Figure 2

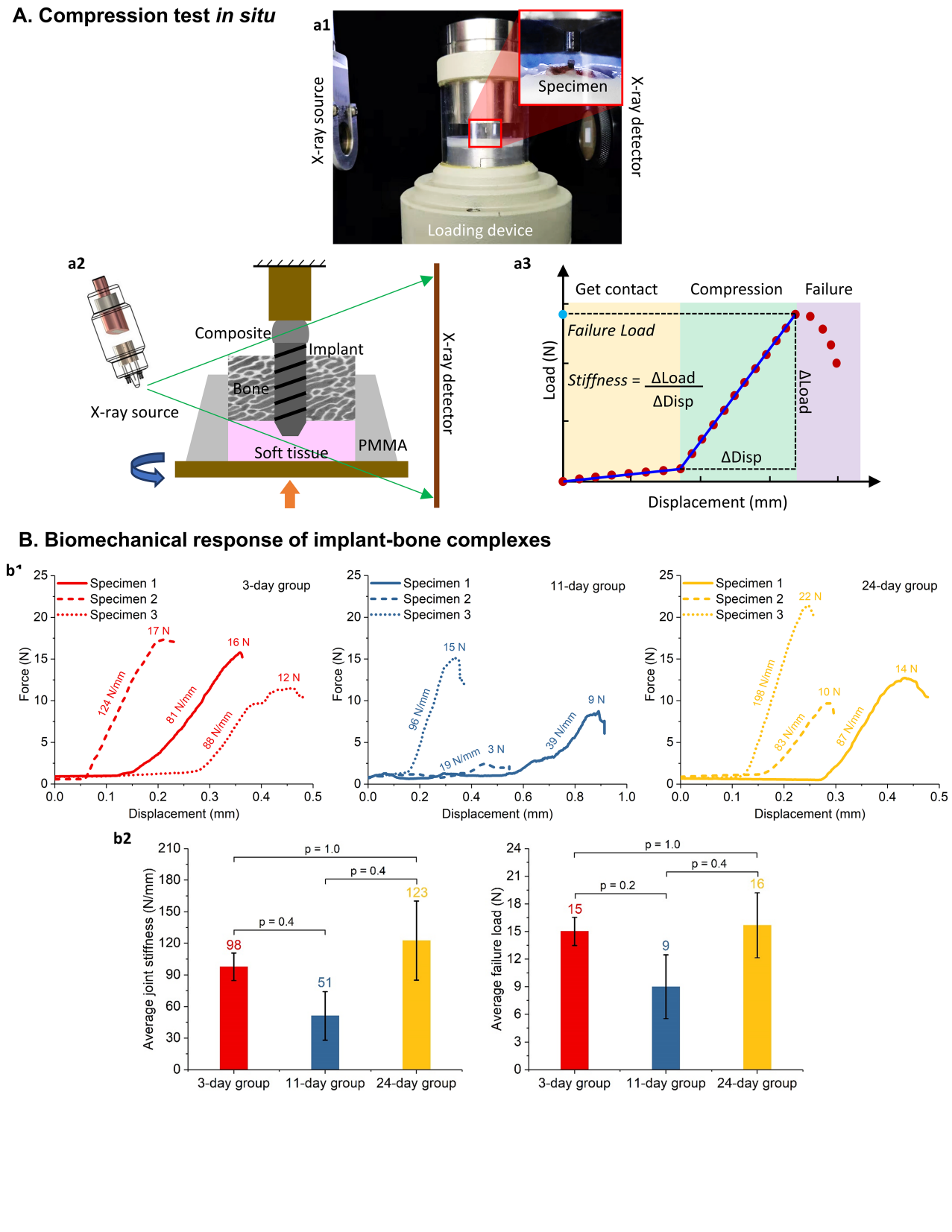
A. Compression test *in situ*
a1
X-ray source
Specimen
X-ray detector
Loading device
a2
Composite
Implant
Bone
X-ray source
Soft tissue
PMMA
X-ray detector
a3
Get contact
Compression
Failure
Failure Load
Stiffness = ΔLoad / ΔDisp
ΔLoad
ΔDisp
Load (N)
Displacement (mm)
B. Biomechanical response of implant-bone complexes
b1
Specimen 1
Specimen 2
Specimen 3
3-day group
11-day group
24-day group
Force (N)
Displacement (mm)
17 N
16 N
12 N
124 N/mm
81 N/mm
88 N/mm
15 N
9 N
96 N/mm
19 N/mm
3 N
39 N/mm
22 N
14 N
10 N
198 N/mm
83 N/mm
87 N/mm
b2
Average joint stiffness (N/mm)
p = 1.0
p = 0.4
p = 0.4
98
51
123
3-day group
11-day group
24-day group
Average failure load (N)
p = 1.0
p = 0.4
p = 0.2
15
9
16

Figure 3

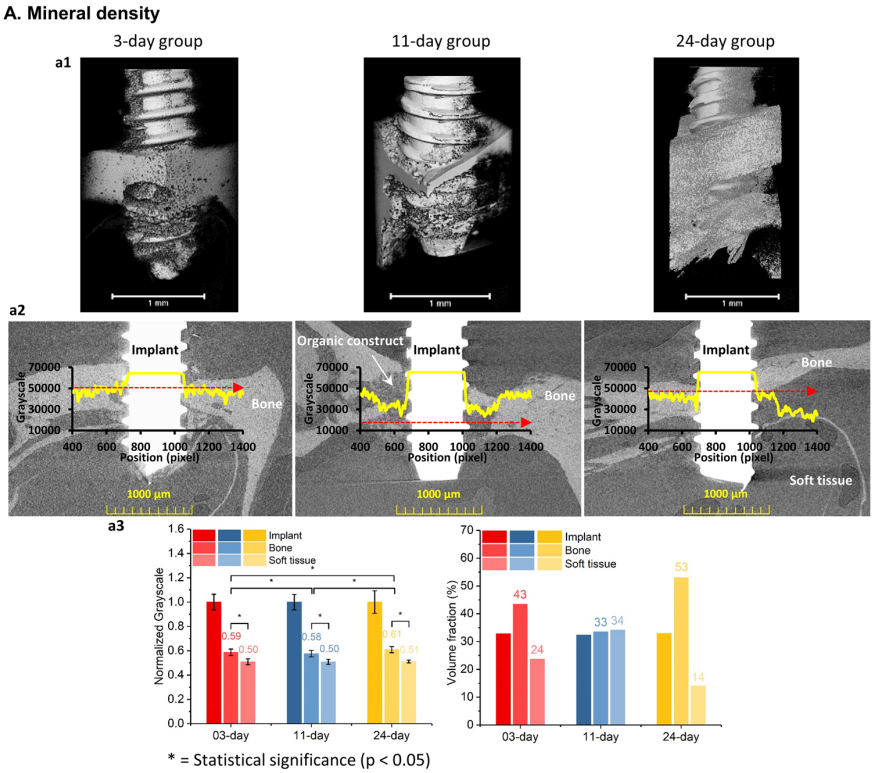
A. Mineral density
3-day group
11-day group
24-day group
a1
1 mm
a2
Implant
Bone
Organic construct
Soft tissue
Grayscale
Position (pixel)
1000 µm
a3
Implant
Bone
Soft tissue
Normalized Grayscale
Volume fraction (%)
0.59
0.50
0.58
0.50
0.61
0.51
43
24
33
34
53
14
03-day
11-day
24-day
* = Statistical significance (p < 0.05)

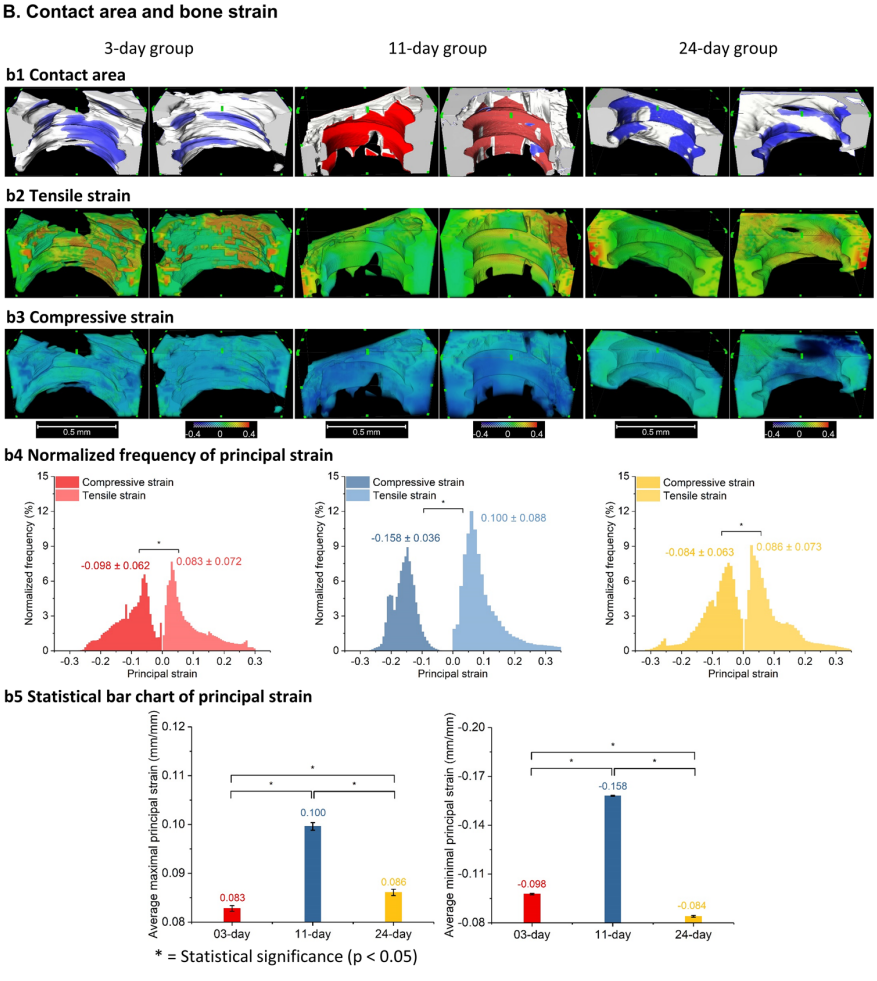
B. Contact area and bone strain
3-day group
11-day group
24-day group
b1 Contact area
b2 Tensile strain
b3 Compressive strain
0.5 mm
b4 Normalized frequency of principal strain
Compressive strain
Tensile strain
Normalized frequency (%)
Principal strain
-0.098 ± 0.062
0.083 ± 0.072
-0.158 ± 0.036
0.100 ± 0.088
-0.084 ± 0.063
0.086 ± 0.073
b5 Statistical bar chart of principal strain
Average maximal principal strain (mm/mm)
Average minimal principal strain (mm/mm)
0.083
0.100
0.086
-0.098
-0.158
-0.084
03-day
11-day
24-day
* = Statistical significance (p < 0.05)

Figure 4

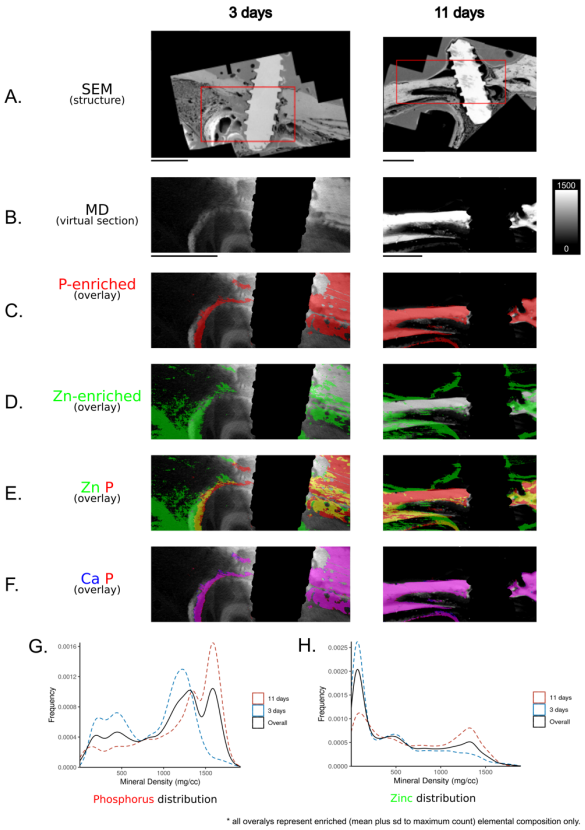

* all overalys represent enriched (mean plus sd to maximum count) elemental composition only.

Figure 5

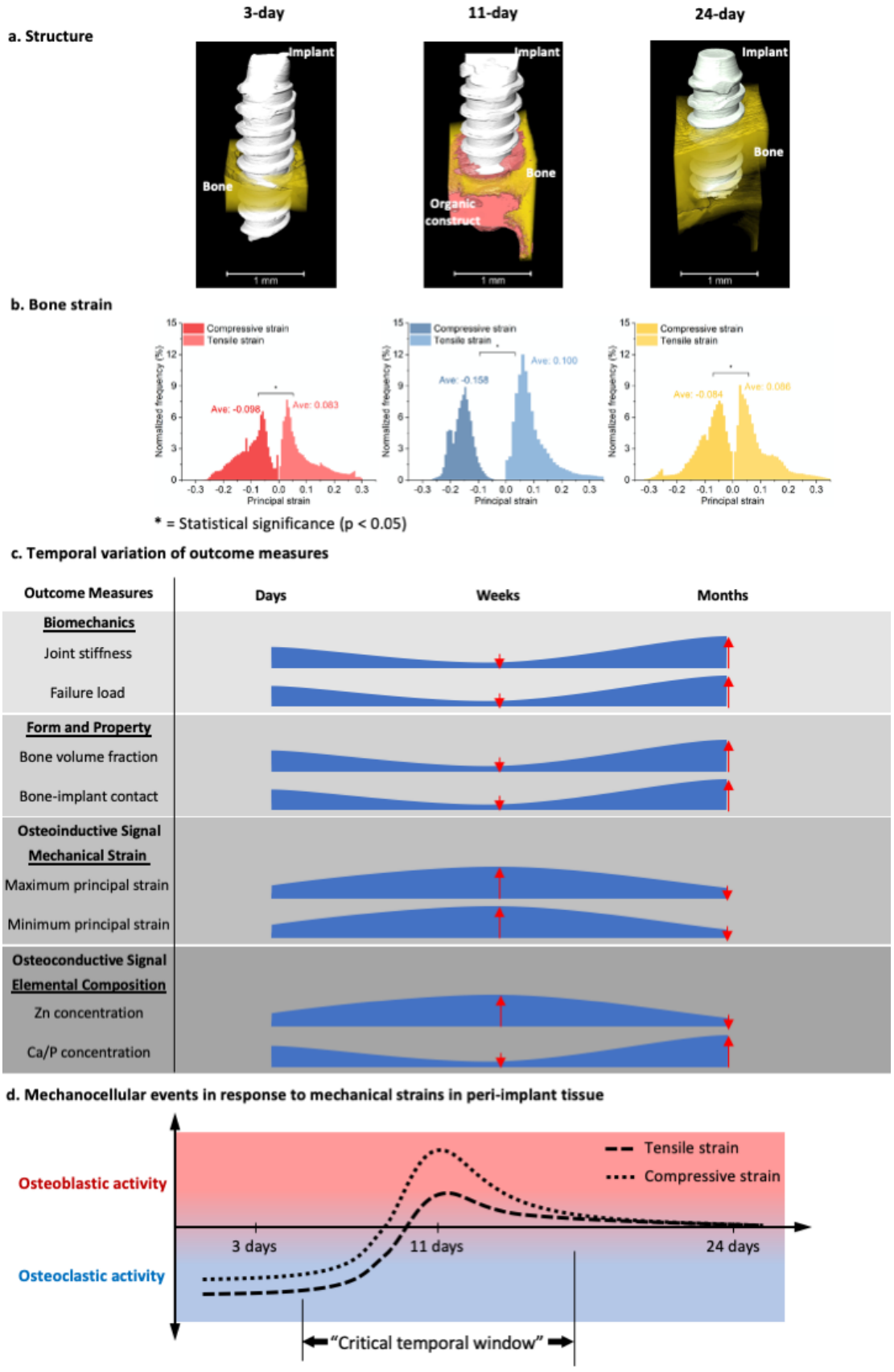
a. Structure
3-day
11-day
24-day
Implant
Bone
Organic construct
1 mm
b. Bone strain
Compressive strain
Tensile strain
Normalized frequency (%)
Principal strain
Ave: -0.098
Ave: 0.083
Ave: -0.158
Ave: 0.100
Ave: -0.084
Ave: 0.086
* = Statistical significance (p < 0.05)
c. Temporal variation of outcome measures
Outcome Measures
Days
Weeks
Months
Biomechanics
Joint stiffness
Failure load
Form and Property
Bone volume fraction
Bone-implant contact
Osteoinductive Signal
Mechanical Strain
Maximum principal strain
Minimum principal strain
Osteoconductive Signal
Elemental Composition
Zn concentration
Ca/P concentration
d. Mechanocellular events in response to mechanical strains in peri-implant tissue
Osteoblastic activity
Osteoclastic activity
Tensile strain
Compressive strain
3 days
11 days
24 days
"Critical temporal window"

Figure Captions

Figure 1. Rendered volumes from X-ray tomograms illustrate location of implant in the jaw bone of a rat. (a) Implant within the hemi-maxilla; (b) Relative position of the dental implant with respect to bone and molar; (c) Implant within maxillary jaw bone.

Figure 2. Compression test *in situ* (A) and biomechanics of the implant-bone complex (IBC) (B). (a1) Experimental setup illustrates a loading device inside a micro X-ray CT system; (a2) Specimen placement during *in situ* compression test; (a3) Schematic of a load-displacement curve of highlights failure load and stiffness of an IBC. (b1) The load-displacement curve of IBC (left: 3-day following implantation, middle: 11-day, right: 24-day); (b2) Differences between stiffness values and failure loads of IBC from the three time groups (left: stiffness, right: failure load). Note: Although the IBC stiffness and failure values are different, no statistical significance in the values across groups was observed because of the small sample size (N = 3).

Figure 3. Grayscale images represent mineral density (A), contact area and bone strain (B) within the peri-implant tissue (left: 3-day group, middle: 11-day group, right: 24-day group): (a1) 3D-rendered volumes of implant-bone complexes; (a2) 2D virtual sections and line profiles illustrate gray scale variations representative of mineral density differences across groups; (a3) Comparison of gray scale intensities and volume fraction values of peri-implant tissue across all three groups. (b1) Area of contact made by peri-implant tissue (red: contact area with bone and organic construct, blue: contact area with mineralized bone); (b2) Maps of maximal principal strain (tensile strain) in peri-implant tissue; (b3) Maps of minimal principal strain (compressive strain) in peri-implant tissue; (b4) Normalized frequency of principal strain in peri-implant tissue; (b5) Bar chart showing statistic value of maximal principal strain (left) and minimal principal strain (right) across time groups. Note: Organic tissue within the heterogeneous peri-implant tissue was also included in maximum and minimum strain calculations.

Figure 4. Correlative maps of peri-implant tissue structure (a) and co-localization of elements (c-f) within higher and lower mineral density regions (b) of the implant-bone complex (IBC). (a) Structure of the IBC using a higher resolution scanning electron microscope (SEM) illustrates organic and inorganic tissues within the peri-implant tissue of any IBC and these observations were time-point-specific. (b) Corresponding virtual sections representative of the electron micrographs illustrate lower (darker gray) and higher (lighter gray) mineral density regions. (c, e, f) Higher phosphorus (P) counts were observed in zinc (Zn)-enriched regions and calcium (Ca)-enriched regions. (d, g, h) Similarly, higher expression of P and Zn was observed in lower mineral density regions as well as higher mineral density regions regardless of time point at which the IBC was harvested. Note: Mineral density is expressed as gray scale.

Figure 5. Spatiotemporal strains based on functional biomechanics of the peri-implant tissue and plausible cellular mechano-responses. (a) Mineral density-segmented volumes illustrate predominantly organic and inorganic compartments within the peri-implant tissue. (b) Normalized frequency of maximum and minimum principal strains corresponds to respective tensile and compressive strains in organic and inorganic compartments of the peri-implant tissue. (c) Temporal variations of various outcome measures from functional biomechanics of implant-bone complex. Polygonal shapes illustrate deviation of outcome measures from the 3-day time group. Arrows represent increase and/or decrease in the respective outcome measure relative to the 3-day time point. (d) Graph highlights plausible mechano-cellular events that permit “functional osteointegration” of the implant following implantation in jaw bone of a rat.